ORIGINAL PAPER

Investigation of structural, optical, and electrical properties of LiMg$_2$Fe$_3$O$_7$ spinel ferrite

Abd daim Jeidd[1] · Amira Bougoffa[1] · A. Benali[1,2,3] · A. Trabelsi[1] · E. Dhahri[1] · K. Khirouni[4] · B. F. O. Costa[2]

Abstract

The $LiMg_2Fe_3O_7$ compounds were prepared by via the citrate process and sintered at two different temperatures to study their effect on structural, morphological, optical, and electric properties. The X-ray diffraction analysis revealed that both samples crystallized in a cubic spinel structure belonging to space group $Fd\bar{3}m$. Increasing the sintering temperature led to an increase in the grain size as characterized by SEM. The UV–visible spectroscopy revealed that the band gap is 2.5eV and 2.35eV for $Mg700$ and $Mg1100$, respectively, which confirm that these compounds are potential candidates for optoelectronics. The electrical resistance was found to decrease with the increase in the sintering temperature, consequently leading to a rise in conductivity.

Keywords Spinel · Sintering temperature · Band gap · Resistance · Conductivity

Introduction

Ferrite spinels with the chemical formula MFe_2O_4, where M is a divalent metal cation, have attracted the interest of researchers in recent years thanks to their good biocompatibility and low toxicity [1, 2]. These materials are widely used as magnetic materials [3–5], adsorbents [6], contrast agents in magnetic resonance imaging (MRI) [7], biosensor systems [8, 9], optics [10], electronics [11], catalysts and photocatalysts [12–14], cancer treatment [15], drug delivery [16], antimicrobial systems [17], and so on. A variety of chemical methods can be used to obtain spinel magnetic nanoparticles: sol–gel synthesis, synthesis in microemulsions, coprecipitation method, hydrothermal method, sonochemical methods [10,

18–20]. Several factors, such as the synthesis method, the substitution process, and the sintering temperature, can significantly modify the electrical and dielectric behavior of spinel materials [21]. Bouokkeze et al. have investigated the effect of sintering temperature on structural, optical, elastic, and electrical properties of spinel $LiZn_2Fe_3O_8$. A reduction in the band gap and the energy activation by increasing the sintering temperature were noted and attributed to the increase in the grain size [22]. Nevertheless, Benali et al. proved that the microstructure, dielectric relaxation, and conduction mechanism of $La_{0.8}Ba_{0.1}Ce_{0.1}FeO_3$ oxide show a dependence on heat treatment. Actually, the electrical resistance and the activation energies decrease with the increase in the sintering temperature, leading to the rise in conductivity [23]. It is essential to compare the structure and physical properties of ferrites at the micron and nanoscale ranges, and because of the influence of structural and magnetic disorders at the grain interfaces, samples with lower grain sizes may have richer electrical and magnetic features [24–27]. Massoudi et al. have suggested that the size of particles has a pronounced effect on physical properties in $Ni_{0.6}Zn_{0.4}Al_{0.5}Fe_{1.5}O_4$ ferrite nanoparticles (NPs). Their results have revealed that the electrical resistivity of the Ni–Zn-Al nano-ferrites decreases with the increase in particle size [24]. Li ferrite ($Li_{0.5}Fe_{2.5}O_4$) belongs to the spinel ferrites family, which is well-known for its use in magnetic, magnetooptical, nano-biomedical, nano-photocatalysts, and magnetodielectric devices due to low

✉ Abd daim Jeidd
  abddayem.jeyid@gmail.com

1 Laboratory of Applied Physics, Faculty of Sciences of Sfax, University of Sfax, B. P. 1171, 3000 Sfax, Tunisia

2 Physics Department, University of Coimbra, CFisUC, Rua Larga, P-3004-516 Coimbra, Portugal

3 I3N, Physics Department, University of Aveiro, Campus de Santiago, Aveiro, Portugal

4 Laboratoire de Physique Des Matériaux Et Des Nanomatériaux Appliquée À L'Environnement, Faculté Des Sciences de Gabes Cite Erriadh, Université de Gabes, 6079 Gabes, Tunisia

dielectric loss, high saturation magnetization, square hysteresis loop, low cost and environment friendliness, and non-toxicity [26–28]. The introduction of metals transition ions leads to the significant variations of physical properties depending on the method of synthesis and doping concentration [29]. Shirsath et al. have reported the decrease in permeability and decrease in saturation magnetization with Co^{+2} substitution in $Li_{0.5}Fe_{2.5}O_4$ [30]. Oxygen vacancy is one of the primordial factors that can improve the oxide material properties especially magnetic properties [30, 31], photocatalytic [32], and gas sensor applications [33]. However, most of the studies carried out on spinel ferrite materials focus on the stoichiometry oxygen materials (AB_2O_4). For this reason, in our research work, we have decided to substitute a portion of iron ions with a monovalent ion (Li) in order to create oxygen deficiency with an automatic manner ($Li_{0.5}MgFe_{1.5}O_{3.5}$). The obtained findings suggested that sintering temperature could effectively control the electric and optical properties of Li-Mg ferrite (grain size effect). To the best of our knowledge, these analyses of the spinel $LiMg_2Fe_3O_7$ at various particle sizes have not been performed before. The combination of conductivity and impedance formalism explains the transport properties in detail. The present research focuses mainly on how sintering temperature affects the structural, morphological, optical, and electric properties of single-phase Li-Mg ferrite spinel. So far, the electric property that has been under-examined requires further research. Thus, the current work aims to investigate the electric properties with the aim of providing researchers with a comprehensive view of the Li-Mg spinel ferrite oxide behavior, which may be useful in a variety of applications such as uncooled infrared bolometric, optoelectronics, photovoltaics, and gas sensor applications.

In this context, the present research work undertook an investigation of the effect of sintering process on the structural, morphological, optical, and electrical properties of the ferrite material $LiMg_2Fe_3O_7$ synthesized by the citrate process. From the impedance spectroscopy measurements, we discussed the evolution of the electrical properties of this material under the variation of the sintering temperature by referring to the analysis of the optical properties. Thus, the examination of ac-conductivity is used to understand the evolution of the electrical behavior and conduction process of the prepared material with the variation of frequency and temperature.

Experimental

Material synthesis

All the chemical reactants in this work were purchased from Sigma-Aldrich and used without further purification. The nitrates $Mg(NO_3)_2.6H_2O$, $Fe(NO_3)_3.9H_2O$, and $LiNO_3$ of purity (99.99%) were used as precursors to synthesize $LiMg_2Fe_3O_7$ powder using the citrate process [34]. All quantities were dissolved in 100 ml of distilled water. Then we mixed this solution with citric acid ($C_6H_8O_7$) with a 1:1.5 molar ratio of the metal cation (Fe + Mg + Li). The resulting mixed solution was magnetically stirred under magnetic stirring at 80 °C until the formation of a viscous gel. The resulting gel was heated on a hot plate at 300 °C to obtain a dark powder. Finally, the burnt ferrite powders were pelletized and sintered separately at 700 °C and 1100 °C for 6 h in an electric furnace to obtain two samples of $LiMg_2Fe_3O_7$ with different particle sizes.

The phase purity and crystal structure of these ferrites were determined by X-ray diffraction (XRD) at room temperature using a Bruker D8 Advance diffractometer with CuK_α radiation (λ=1.5406 Å). The acquisition was in the 2θ range of 10–100° with a step of 0.02° and acquisition time for each step of 1 s. The characterization of the surface morphology and the chemical compositions of the synthesized samples were studied using a Merlin scanning electron microscope (SEM) Hitachi S3500 Microanalysis EDS, Kevex (132 keV) equipped with a microanalyzer at energy dispersive X-rays (EDX). Absorption spectra were obtained at room temperature using a Shimadzu UV-3101PC scanning spectrophotometer. The electrical characterization was carried out by impedance spectroscopy using an Agilent 4294A impedance analyzer.

Results and discussion

Structural properties

Figure 1a–b show the X-ray diffraction of the $LiMg_2Fe_3O_7$ samples annealed at 700 °C and 1100 °C. The reflections of the atomic planes (111), (220), (311), (222), (400), (331), (422), (511), (440), and (442) are identified. As the sintering temperature increases, the peak width decreases due to an increase in crystallite size. Rietveld refinement by FULLPROF software [35] confirms the formation of a cubic spinel structure with the $Fd\bar{3}m$ space group, without any additional peaks of a secondary phase. The refinement parameters for the two prepared samples are listed in Table 1. We observed a low-quality value of χ^2 suggesting that the sample refinement is efficient and that the samples are of good quality. The quantitative analysis proves that the chemical compositions of Mg700 and Mg1100 samples are $[Li_{0.487}Fe_{0.382}Mg_{0.131}]_A[Fe_{1.115}Mg_{0.885}]_BO_{3.505}$ and $[Li_{0.487}Fe_{0.362}Mg_{0.151}]A[Fe_{1.13}Mg_{0.870}]BO_{3.5}$, respectively.

In our present work, the lattice parameters (a) and (V) increase with the increase of the sintering temperature. This is similar with other ferrite systems in the literature which show that the lattice parameters increase as a function of the
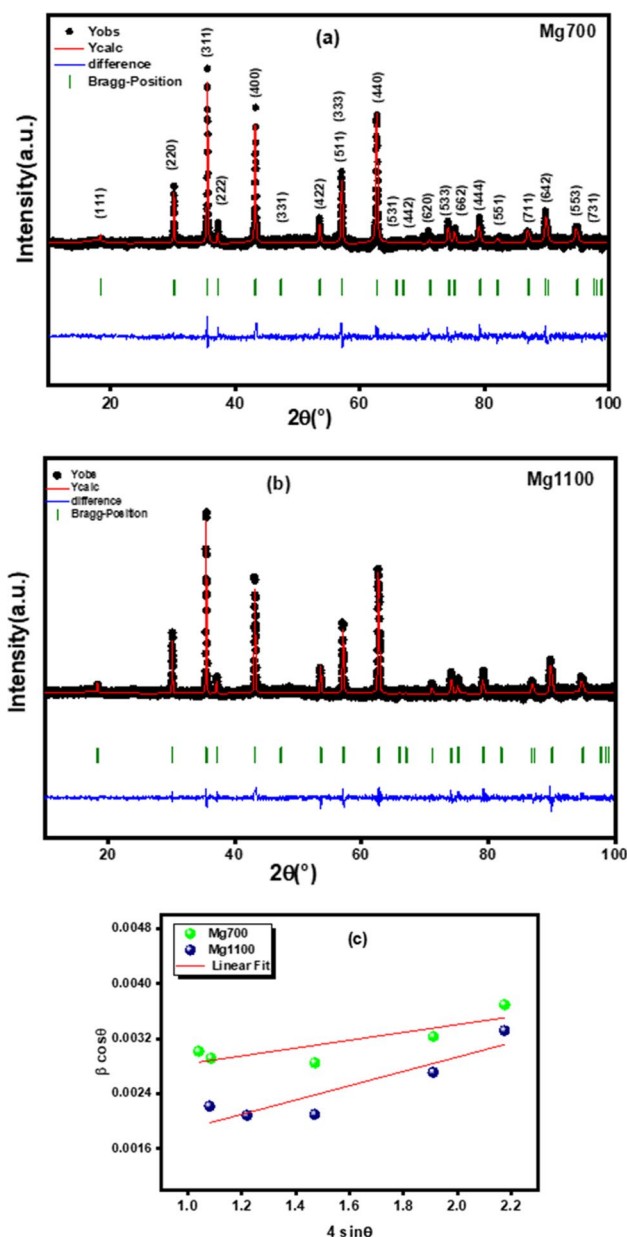
Fig. 1 **a–b** Refined XRD patterns of the two samples, Mg700 and Mg1100, **c** Williamson–Hall plots of Mg700 and Mg1100

size by Williamson–Hall (D_{WH}) method, which gives a linear relationship between $\beta\cos\theta$ and $4\varepsilon\sin\theta$ as shown in Fig. 1b. The ordinate at the origin of the line gives the size of the crystallites D_{WH} while the slope gives the induced strain ε. The calculations carried out in this section are based on the model of Williamson–Hall which takes account of the possible stresses in the material and that of Scherrer which neglects some constrains [41]. The lattice microstrain of each sample obtained using the Williamson–Hall method has a positive value, indicating lattice expansion. This observed difference between the calculated crystallites size using both methods is linked to the strain effect which is not taken in account in Scherrer method (Table 2).

As shown in Table 1, increasing the size of the crystallites decreases the porosity (P), which has the effect of increasing the bulk density (ρ_{exp}), revealing that the temperature of annealing increases the disorder of the spinel ferrite system. We can conclude that the specific surface decreased from 27.08 to 11.41 $m^2 g^{-1}$ with the increase in particle size. However, the high surface area value of $LiMg_2Fe_3O_7$ nanoparticles suggests that $Mg700$ nanoparticles could be used as sensors to detect gases [42]. (Equations used for different calculations are given in the supplementary part.)

Morphology

Scanning electron microscopy (SEM) was used to obtain an accurate estimation of the microstructure and morphology of the nanocrystals. Figure 2a–b show SEM images of two samples, $Mg700$ and $Mg1100$. Both samples exhibited agglomeration, which could be attributed to electrostatic effects as well as an artifact of the drying of aqueous suspensions and the magnetic interaction between nanoparticles, revealing the formation of nearly spherical particles and evenly distributed nanoparticles. Large particle size is observed at a higher sintering temperature $Mg1100$.

The observed skewed distribution can be described using a Lorentz distribution function, as shown in Fig. 2a–b. Based on SEM images and using ImageJ software [43], the average grain size was found to be around 100 and 385 nm for the two samples $Mg700$ and $Mg1100$, respectively. As the sintering temperature increases, the size of the grains increases, which is caused by the coalescence of the crystallites when the temperature increases.

Figure 3a–b illustrate elemental analysis of $Mg700$ and $Mg1100$ samples at room temperature using EDX. The spectrum confirms the presence of all Fe, Mg, and O elements in both synthesized samples, indicating that no integrated element was lost and no contaminant element was introduced during sintering. The outcome (EDX) predicted the required constituent proportion as well as the chemical purity of the samples, indicating a homogeneous chemical composition. The atomic and weight percentage of individual elements for

sintering temperature [36–40]. It can be seen from Table 1 that the value of the length of site A (L_{A-A}) is greater than that of site B (L_{B-B}), which leads to the fact that the electron jump between ions A and B is less probable than that between sites A and B. The X-ray density ρ_{X-ray} deduced from X-ray diffraction decreases as the sintering temperature increases, going from 3.97 g·m^{-3} for $Mg700$ to 3.94 g·m^{-3} for $Mg1100$.

The size of the crystallites calculated by the Scherrer method is 45 and 63 nm for $Mg700$ and $Mg700$, respectively. Equation (5) in the supplementary part calculates crystallite

Table 1 Structural parameters of the two samples Mg700 and Mg1100

Parameters	Mg700	Mg1100
a(Å)	8.3750	8.3777
V(Å^3)	587.4257	587.9877
χ^2	4.892	4.443
R_p(%)	36.9	37.1
R_{wp}(%)	21.1	22.2
Cations distribution	[Li$_{0.487}$Fe$_{0.382}$Mg$_{0.131}$]$_A$ [Fe$_{1.115}$Mg$_{0.885}$]$_B$O$_{3.505}$	[Li$_{0.487}$Fe$_{0.362}$Mg$_{0.151}$]$_A$ [Fe$_{1.13}$Mg$_{0.870}$]$_B$O$_{3.46}$
R_e(%)	9.54	10.5
a$_{exp}$ (Å)	8.3752	8.3778
L$_{A-A}$ (Å)	3.626	3.627
L$_{B-B}$ (Å)	2.961	2.962
L$_{A-B}$ (Å)	3.472	3.473
D_{DS}(nm)	53	72
θ_{A-O-B}(°)	124.8539	124.8718
θ_{B-O-B}(°)	90.5790	90.5514
Tetrahedral bond length (dAE)	2.08325	2.0844
Octahedral bond length (dBE)	1.083152	1.8314
D_{WH}(nm)	61	162
ε	5.68.10^{-4}	4.1.10^{-3}
ρ_{X-ray}(g.cm^{-3})	3.97	3.96
ρ_{exp}(g.cm^{-3})	3.17	3.25
P(%)	20.151	17.929
S(m^{2}g^{-1})	27.08	11.41

Table 2 The experimental proportions of the constituents obtained by EDS and the theoretical ones of the two samples Mg700 and Mg1100

	Mg700 %Atomic		Mg1100 %Atomic	
	Theoretical values	Experimental values (EDX)	Theoretical values	Experimental values (EDX)
C	-	4.48	-	4.08
Li	7.69	-	7.69	-
Mg	15.38	14.90	15.38	13.72
Fe	23.08	24.19	23.08	27.53
O	53.85	56.43	53.85	54.67

both the samples [*Mg*700, *Mg*1100] are also shown in the inset table. The obtained results confirm the stoichiometric amounts of the elements in the prepared compound close to the target chemistry. We have to notice that the small atomic number (Z) of the element lithium, which is lower than the sensitivity of EDX, is the cause of its invisibility in the spectrum [44].

Optical study

UV–visible spectroscopy was used to study the optical properties of the two synthesized samples. Figure 4a shows the absorption spectra of two samples for the UV/visible/IR range. The absorption edges were found to be in the visible region, demonstrating its suitability for visible light. The electronic transition from the valence band to the conduction band can be used to explain the strong absorption ($O_{2p}Fe_{3d}$). In other words, the electronic excitation from the O_{2p} level (valence band) to the Fe_{3d} level (conduction band) absorbed a significant amount of visible light [45].

The band gap energies are calculated by the following Tauc relation [5, 46]:

$$(\alpha h\nu) = A[h\nu - E_g]^n \tag{1}$$

where α is the absorption coefficient, A is a constant reflection of the amorphous solid structure's disorder degree, E_g is the gap energy, $h\nu$ is the energy of the incident photon expressed in (eV), and the value of n denotes the nature of transition (equal 2 or 1/2 according to the electronic transitions are respectively direct or indirect).

As in the literature, $Li_{0.5}Fe_{2.5}O_4$, $LiMg_{0.5}Fe_{2.5}O_4$, and $LiNi_{0.5}Fe_{2.5}O_4$ [29, 47] have direct gap, the synthesized compound has also a direct gap. Besides, the band gap value approximately corresponds to the wavelength (around 500 nm) of the inflexion point in absorbance spectrum. This means that the band gap is around 2.48 eV.

Fig. 2 **a** SEM morphology, grain sizes histogram of Mg700, **b** SEM morphology, grain sizes histogram of the Mg1100
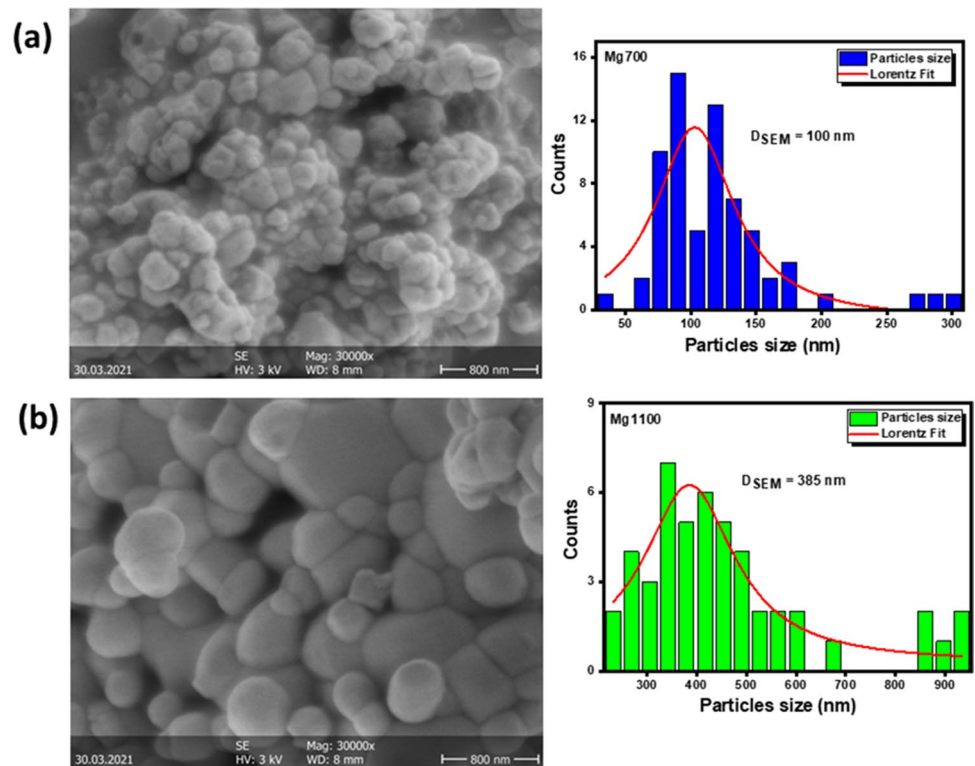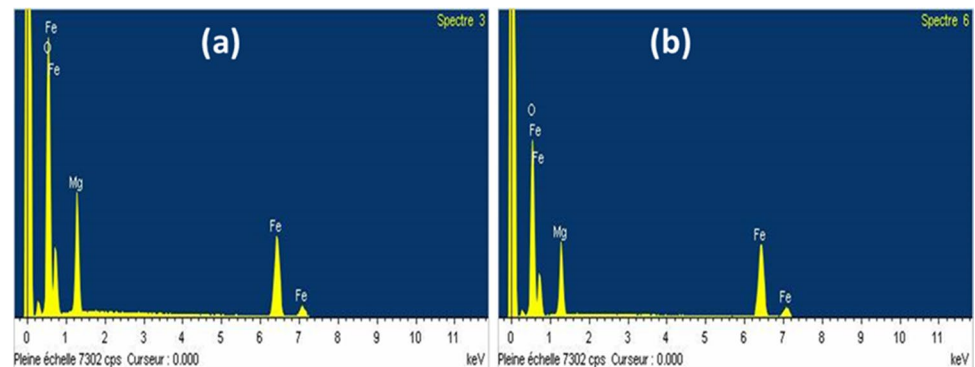

Fig. 3 **a–b** EDX spectrum of the two samples Mg700 and Mg1100

The band gap energies (E_g) are calculated by plotting $[\alpha h\nu]^2$ with the photon energy $[h\nu]$ as shown in Fig. 4b–c. However, the energy (E_g) values are 2.5 and $2.35 eV Mg700$ and $Mg1100$, respectively. This confirms that the compound is direct transition type and indicates that the band gap (E_g) decreased with the increase in the particle size. In this work, the reduction of band gap is probably attributed to the composition and crystal structure of the obtained products. Taking into consideration the Mott and Davis model [48, 49], the disorder degree and the defects created by unsaturated and dangling bonds expand the width of the localized states. These latter, situated near the band gap edge, lead to a decrease of the band gap. These band gap energy values indicate that the two ferrite samples can be applied in several technological fields such as photovoltaics, optoelectronics, and gas sensors [50].

The refractive index (n_0) of semiconductor materials is essential in determining the optical and electrical properties of the crystal. Understanding n_0 n is essential in the design of heterostructure lasers in optoelectronic devices and solar cell applications [51]. Using Moss' empirical relationship [52], the refractive index (n_0) of ferrite nanostructures can be calculated from the value of E_g:

$$E_g n_0^4 = 104 \ eV \tag{2}$$

Additionally, we used Eq. (3) to calculate the high-frequency dielectric constant ε_α with the refractive index [53]:
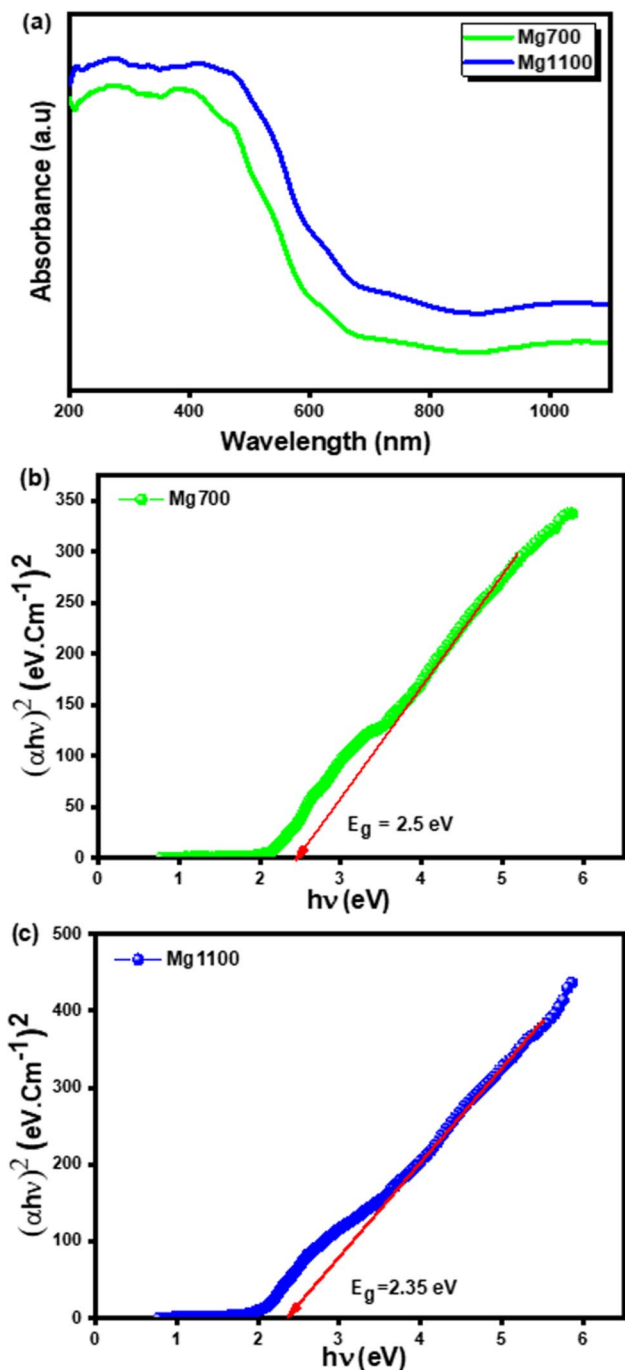
Fig. 4 **a** Absorbance versus wavelength of Mg700 and Mg1100 samples. **b–c** The variation of $(\alpha h\nu)^2$ versus $(h\nu)$ of the two compounds Mg700 and Mg1100

$$\varepsilon_\alpha = n_0{}^2 \tag{3}$$

The values of refractive index (n_0) and high-frequency dielectric constant (ε_α) of the two samples are 2.54, 6.44, 2.57, and 6.65, respectively. Obviously, the refractive indices (n_0) and (ε_α) increased with the increase in the sintering
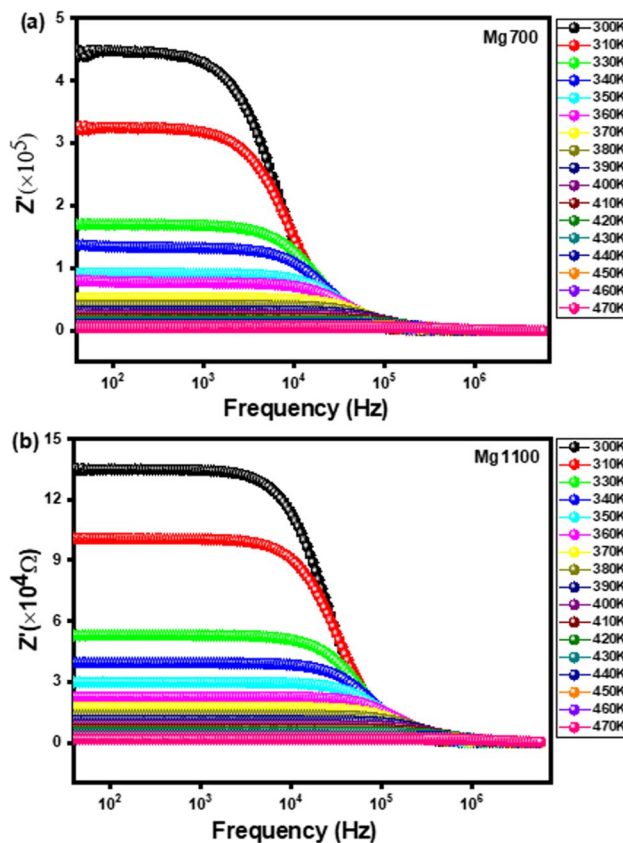
Fig. 5 Real part Z' as a function of frequency at different temperatures of the two compounds Mg700 (**a**) and Mg1100 (**b**)

temperature. The results can be discussed in terms of lack of oxygen with higher sintering temperatures [24].

Complex impedance spectroscopy

Real part of impedance

Figure 5a–b represent the variation of the real part of the impedance (Z') with frequency at different temperatures of the two compounds *Mg*700 and *Mg*1100. These plots show that the values of Z' are higher in the low frequency range. It was also found that Z', whose value decreases with the increase in temperature, is temperature-dependent, indicating an increase in conductivity [54]. At high frequencies, the Z' values become almost frequency-independent with a merging of all Z' curves. In addition, it is important to mention that Z' decreases with the increase in temperature, which can be accredited to the decrease in the density of charge carriers and the increase in their mobility, proving a reduction in the localized character of charge carriers [55, 56]. It is important to note that the value of the real part of the impedance decreases with the increase in the sintering temperature from 700

to 1100 °C, which highlights a decrease of the electrical resistance, and thus an improvement of conductivity.

Imaginary part of impedance

Figure 6a–b show the variation of the imaginary part Z'' of the complex impedance as a function of frequency, at several temperatures for the compounds $Mg700$ and $Mg1100$, respectively. The Z'' spectra of the two compounds are characterized by the appearance of a single peak that shifts towards high frequencies, substantiating the presence of a relaxation phenomenon in the synthesized samples. As a result, an increase in relaxation time and mobility of charge carriers for the jump can be noted, leading to the reduction in the strength of the bulk material [57, 58]. The temperature dependence of the relaxation frequency for each compound was plotted, to calculate the activation energy, according to Arrhenius' law expressed as follows [59]:

$$f = f_0 \exp\left(\frac{E_a}{K_B T}\right) \tag{4}$$

where f_0 is the pre-exponential term, E_a is the activation energy, and K_B is the Boltzmann constant.

The logarithmic variation of f_{max} is plotted against 1000/T in Fig. 6c. The obtained values of activation energy were found to be around $0.321 eV$ for $Mg700$ and $0.318 eV$ for $Mg1100$. It can be concluded that increasing the sintering temperature decreases the activation energy as in the literature [60].

Equivalent circuit

Figure 7a–b illustrate the variation of Z'' as a function of Z' at different temperatures for the two studied compounds. This figure shows a single semicircle corresponding to the grain response, whose diameter decreases with temperature, indicating a thermally activated conduction mechanism [61]. The experimental data of the Nyquist diagram (Z'' as function of Z'') were fitted by the Z-view software. The best fits are obtained by the equivalent circuit combining a grain resistance (R_g) and a fractal capacitance (CPE). A similar behavior is observed in spinel compounds reported in the literature [4, 62, 63]. The parameters obtained are therefore summarized in Table 3.

The impedance is calculated as follows [64]:

$$Z_{CPE} = \frac{1}{Q(j\omega)^\alpha} \tag{5}$$

where $j = \sqrt{-1}$, Q is a proportional factor indicates the value of the capacitance, α is an empirical exponent with values between
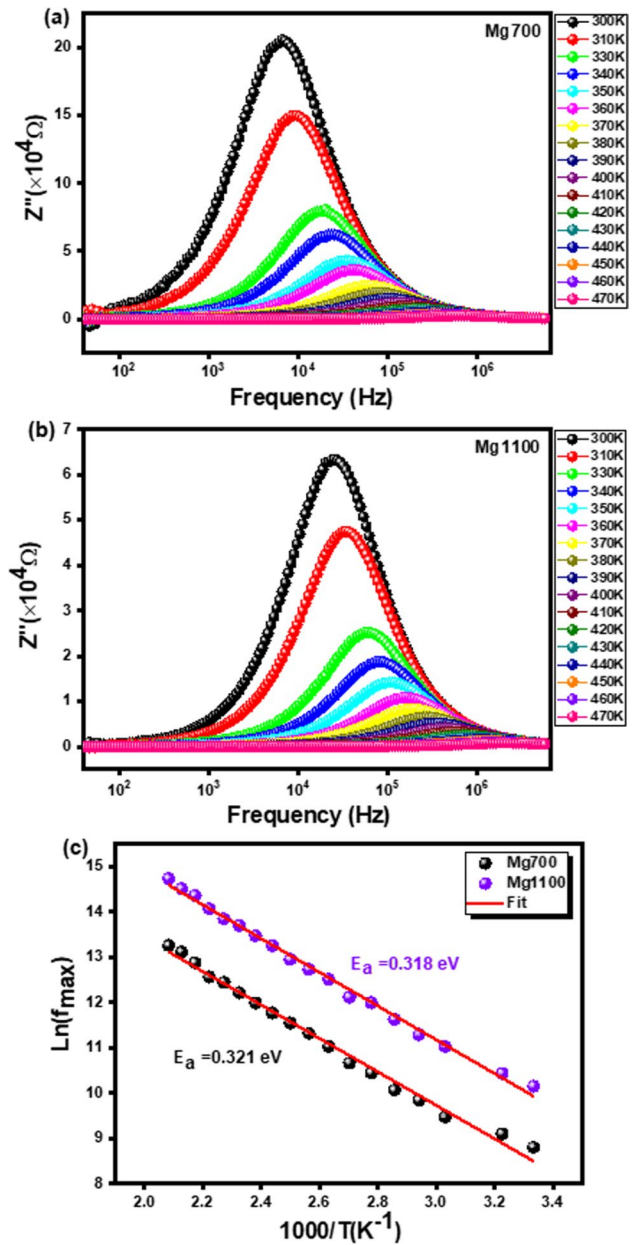

Fig. 6 Plots of the imaginary part of the impedance (Z'') versus frequency at different temperatures of the Mg700 (**a**) and Mg1100 samples (**b**), **c** variation of ln(f$_{max}$) versus 1000/T

0 and 1 indicating the change of the compressed semicircle from an ideal semicircle, and ω is the angular frequency.

Figure 8a shows the variation of grain strength as a function of the temperature of the two samples sintered at 700 and 1100 °C, respectively. It can be clearly seen that the grain resistance values decrease with the increasing temperature of the two compounds, which is due to the increase in the mobility of charge carriers or the decrease in the average energy of the barriers of potential [65, 66].
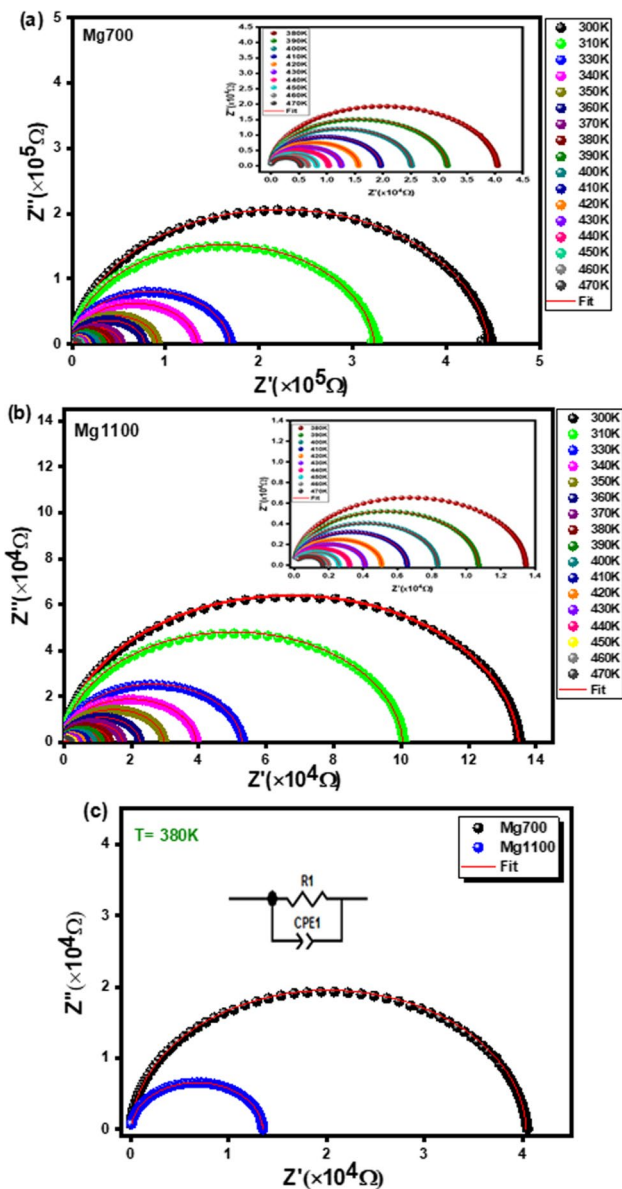
Fig. 7 Nyquist plots of Mg700 (**a**) and Mg1100 (**b**), **c** example of adjustment of the equivalent circuit for the two compounds at $T = 380$ K

The logarithmic variation of the grain strengths (R_g) of the prepared compounds $Mg700$ and $Mg1100$, respectively, can be plotted as a function of $1000/T$ (Fig. 8b) and appears to follow the Arrhenius relation (Eq. 6):

$$R_g = R_0 \exp\left(\frac{E_a}{K_B T}\right) \tag{6}$$

where R_0 is the resistance of the grains, E_a is the activation energy, and K_B is the Boltzmann constant.

As the sintering temperature increases, the values of the activation energies related to the grains decrease, which is

similar to the results obtained for the conductivity and the modulus.

Electrical conductivity

Figure 9a–b show the spectra of conductivity (ac) as a function of frequency at several temperatures, for the $LiMg_2Fe_3O_7$ compounds sintered at 700 and 1100 °C. Conductivity spectra are composed of two distinct frequency regions. At low frequencies in which conductivity behaves almost constantly, it is practically independent of frequency. This region is associated with the long-range translational motion of charge carriers [67]. In the second frequency region, the electrical conductivity increases with the increase in frequency following Jonscher's power law [54, 68]:

$$\sigma_{ac}(\omega) = \sigma_{dc} + A\omega^s \tag{7}$$

where σ_{ac} is the direct current conductivity, ω is the angular frequency, s is an exponent depending on the temperature that presents the degree of interaction between mobile ions and the lattices around them [57], and A is a constant pertaining to the strength of polarizability.

Figure 9c and d show an example of fitting the σ_{aC} data to $T = 380$ K for the two compounds Mg700 and Mg1100 which proves a good agreement between the theoretical and experimental data.

Also, the temperature dependence of the exponent s for the $Mg700$ and $Mg1100$ samples is shown in Fig. 10a–b. The $Mg700$ compound shows a conduction process polaron tunneling model (OLPT), and $Mg1100$ exhibits s values, which increase with increasing temperature, confirming the conduction process non-overlapping small polaron tunneling model (NSPT).

Figure 11a–b show the continuous variation of conductivity with temperature (a), and the plot of $\ln(\sigma_{dc}.T)$ as a function of $1000/T$ (b). Figure 11a shows the continuous variation of conductivity with temperature. This figure shows that the conductivity of samples annealed at 700 and 1100 °C increases steadily with temperature, indicating the characteristics of semiconductors. This could be because increasing the sintering temperature improves the compactness of the specimens [27, 69].

To determine the activation energy of our samples, we used the model of small polaron hopping (SPH) at high temperature expressed by the following expression [70, 71]:

$$\sigma_{dC}T = \sigma_0 \exp\left(-\frac{E_a}{K_B T}\right) \tag{8}$$

where σ_0 is a pre-exponential factor, E_a is the activation energy, and K_B is the Boltzmann constant.

Table 3 The electrical parameters of the Mg700 and Mg1100 samples extracted by using an equivalent circuit adjustment

| T(K)	R_g (kΩ)		CPE$_1$ ($\times 10^{-11}$ Ω^{-1}s$^\alpha$)		α	
	Mg700	Mg1100	Mg700	Mg1100	Mg700	Mg1100
300	446	135	9.431	6.886	0.951	0.967
310	101	101	6.782	6.782	0.962	0.968
330	52.99	52.9	7.156	7.156	0.975	0.972
340	39.3	39.3	6.973	6.973	0.955	0.974
350	91.3	29.7	6.850	6.850	0.967	0.976
360	71.0	22.5	5.951	5.951	0.970	0.978
370	52.1	17.4	6.572	6.572	0.977	0.979
380	40.4	13.5	6.563	5.648	0.978	0.982
390	31.5	10.7	6.537	5.564	0.978	0.983
400	25.1	8.34	6.538	5.390	0.978	0.985
410	19.6	6.57	6.501	5.511	0.979	0.983
420	15.6	5.09	6.510	5.443	0.979	0.984
430	12.6	4.12	6.521	5.483	0.979	0.9836
440	10.3	3.22	6.547	6.156	0.979	0.9826
450	8.19	2.60	6.489	6.227	0.9798	0.982
460	6.61	2.00	6.417	6.338	0.981	0.980
470	5.35	1.67	6.353	6.518	0.981	0.978
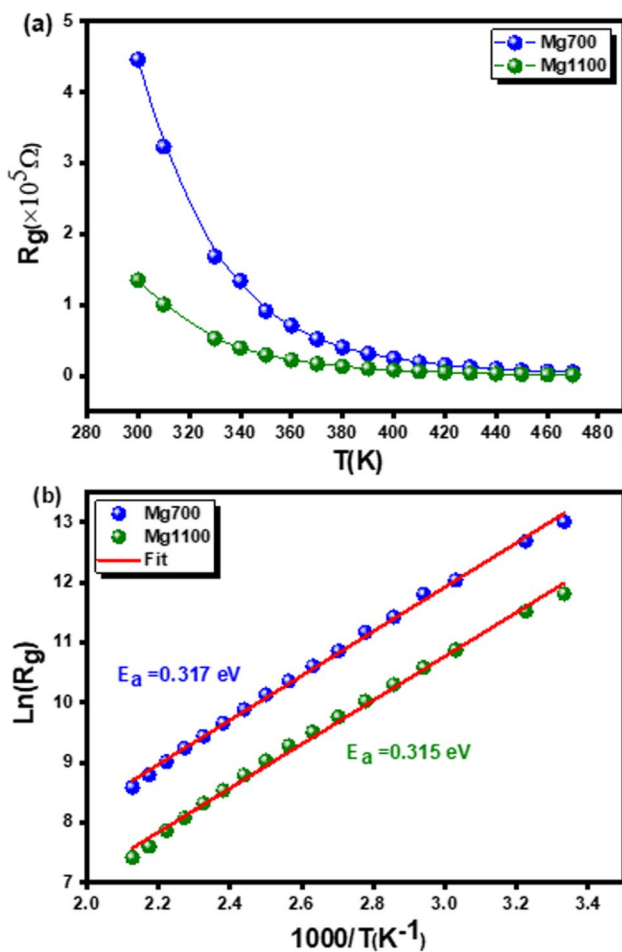
Fig. 8 **a** Grain resistance plots as function of temperature, **b** variation of ln(R_g) versus (1000/T) from the two samples Mg700 and Mg1100

From Fig. 11b, the activation energies determined are $E_a = 0.352 eV$ for $Mg700$ and $E_a = 0.347 eV$ for $Mg1100$, respectively. It has been found that as the sintering temperature increases, the activation energy decreases, and the conductivity increases. These findings are in good agreement with the decrease of the grain resistance proved by the equivalent circuit simulation. As already noted, the electrical conductivity enhancement is due not only to the increase of the density of charge carriers but also to the decrease of the porosity in the structure after the increase in the sintering temperature [69]. Moreover, we detected the same value of the activation energies with those extracted from the impedance, electrical modulus, and grain resistance data.

In the literature, numerous investigations have shown that the grain boundaries of nanostructured materials play an important role in their transport and dielectric properties [27, 72, 73]. From the SEM results, the microstructure of the prepared structure is formed by conductive grains separated by resistive grain boundaries. Such behavior will undoubtedly affect the conductivity and dielectric properties of the studied system. In the present work, the annealing temperature increase induces changes in various parameters like the intra-grain distance, the number, and the size of the grains. Accordingly, the annealing temperature increase is accompanied by an increase in the grain size and a decrease in the number of grains, which enhances the electrical conductivity of the studied system.
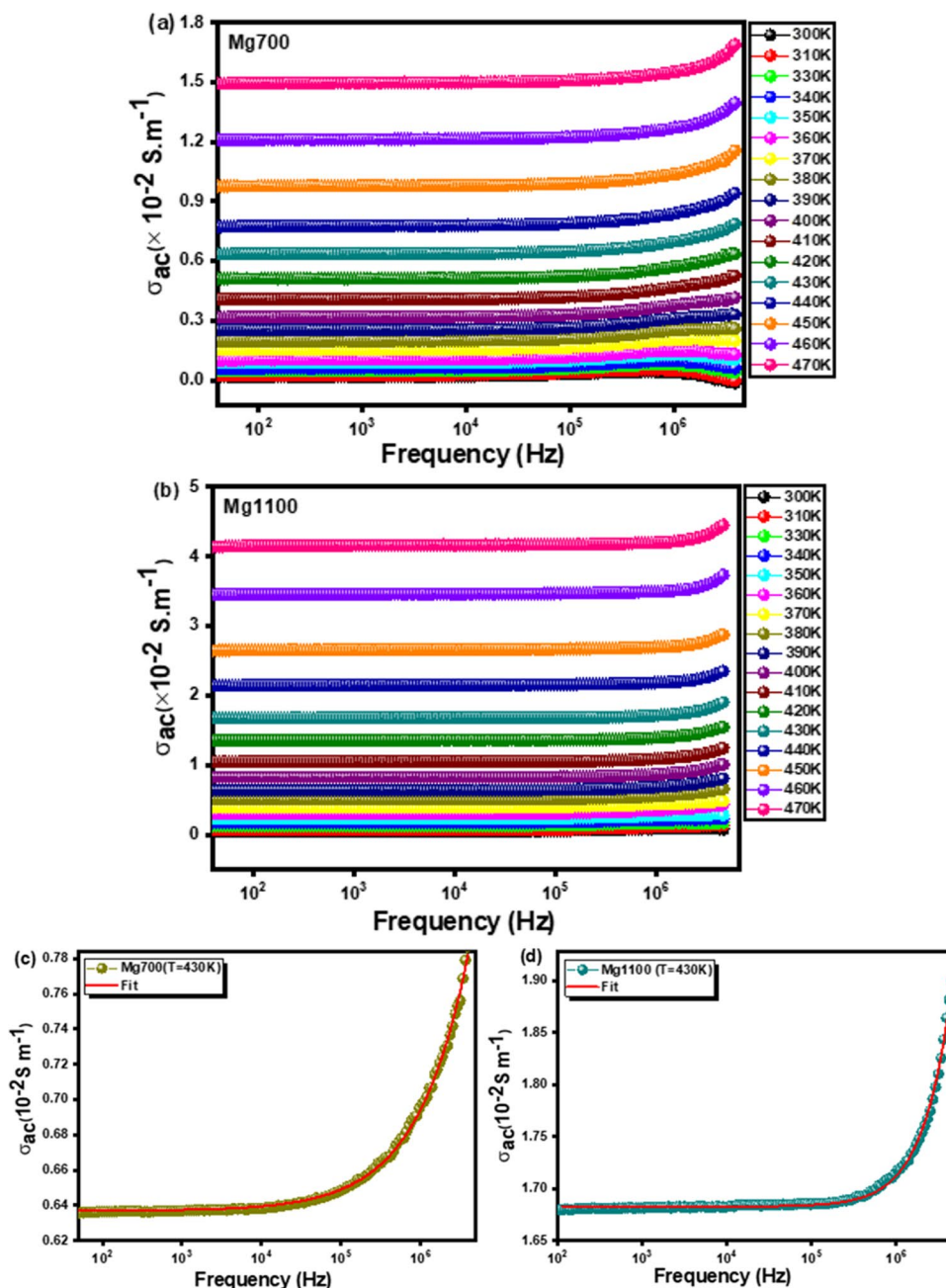
Conclusion

The ferrite material $LiMg_2Fe_3O_7$ was successfully synthesized by the citrate process and the obtained nanoparticles were treated separately at two different sintering temperatures, namely 700 and 1100 °C. The morphology of the two samples was analyzed by SEM, which showed that the grains were composed of different crystallites. Besides, the EDX analysis confirmed the purity of the samples. The electrical characterization of $LiMg_2Fe_3O_7$ sintering at 700 and 1100 °C allowed us to

conclude that increasing the temperature improves the electrical conductivity. The sample annealed at 1100 °C has the highest conductivity and the lowest activation energy. The conduction mechanism of conduction mechanism was charge carrier hopping between ions of different valence states. The variation of the exponent s as a function of temperature shows the presence of two conduction models, large polaron tunneling model (OLPT) and non-overlapping small polaron tunneling model (NSPT) for $Mg700$ and $Mg1100$, respectively. The activation energies were calculated from the conduction of the imaginary part of
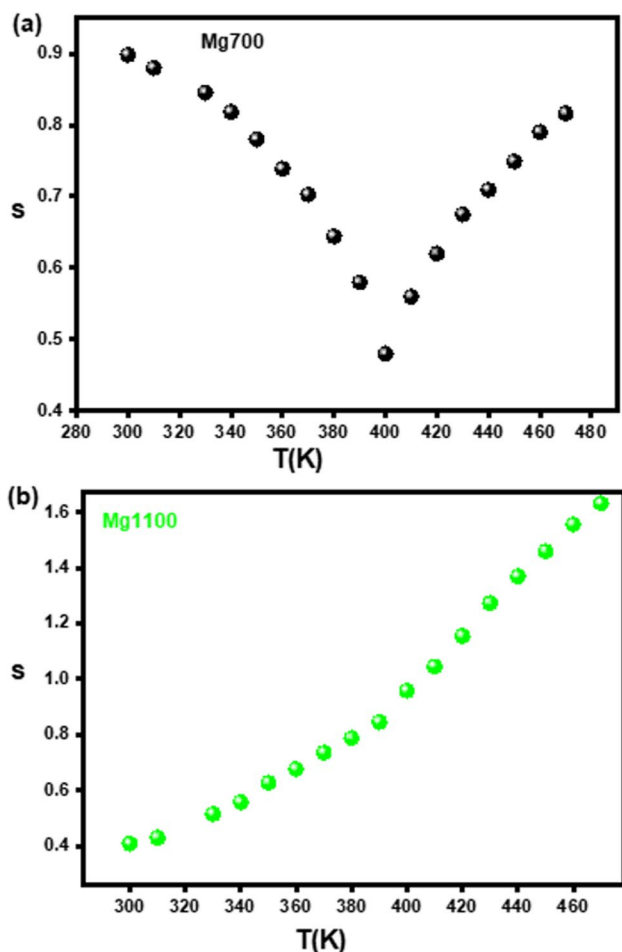
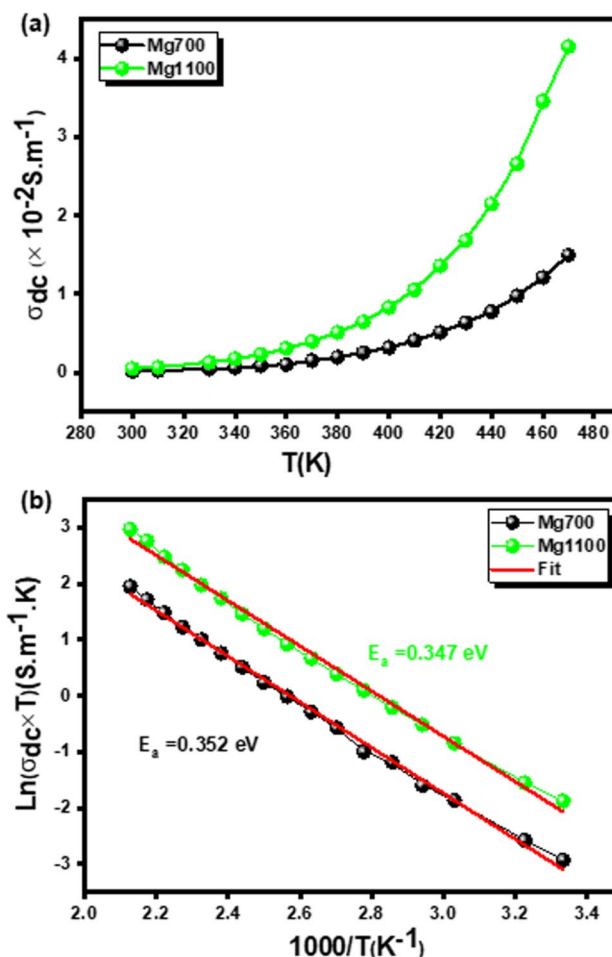**Fig. 10** The variation of the exponent "s" as a function of temperature of Mg700 (**a**) and Mg1100 (**b**) samples

Fig. 11 Variation of the exponent σ_{dc} as function of temperature function of Mg700 (**a**) and Mg1100 (**b**) samples, **c** variation of $\ln(\sigma_{dc})$ versus 1000/T of the two samples

the impedance, resistance of the grains, alternating current dc, and imaginary part of the modulus and conformed that the electric and dielectric have and the same professed.

References

1. Zhang Y, Yang Z, Yin D et al (2010) Composition and magnetic properties of cobalt ferrite nano-particles prepared by the co-precipitation method. J Magn Magn Mater 322:3470–3475
2. Gharibshahian M, Mirzaee O, Nourbakhsh MS (2017) Evaluation of superparamagnetic and biocompatible properties of mesoporous silica coated cobalt ferrite nanoparticles synthesized via microwave modified Pechini method. J Magn Magn Mater 425:48–56
3. Raghuvanshi S, Kane SN, Tatarchuk TR, Mazaleyrat F (2018) Effect of Zn addition on structural, magnetic properties, anti-structural modeling of Co1−xZnxFe2O4 nano ferrite. Bikaner, India, p 030055
4. Ahmed MA, Hassan HE, Eltabey MM et al (2018) Mössbauer spectroscopy of MgxCu0. 5-xZn0. 5Fe2O4 (x= 0.0, 0.2 and 0.5) ferrites system irradiated by γ-rays. Physica B 530:195–200
5. Tatarchuk T, Bououdina M, Macyk W et al (2017) Structural, optical, and magnetic properties of Zn-doped CoFe2O4 nanoparticles. Nanoscale Res Lett 12:1–11
6. Reddy DHK, Yun Y-S (2016) Spinel ferrite magnetic adsorbents: alternative future materials for water purification? Coord Chem Rev 315:90–111
7. Ahmad T, Bae H, Iqbal Y et al (2015) Chitosan-coated nickel-ferrite nanoparticles as contrast agents in magnetic resonance imaging. J Magn Magn Mater 381:151–157
8. Yang M, Jeong J-M, Lee KG et al (2017) Hierarchical porous microspheres of the Co3O4@ graphene with enhanced electrocatalytic performance for electrochemical biosensors. Biosens Bioelectron 89:612–619
9. Zhao M, Fan S, Liang J et al (2015) Synthesis of mesoporous grooved ZnFe2O4 nanobelts as peroxidase mimetics for improved enzymatic biosensor. Ceram Int 41:10400–10405
10. Tatarchuk T, Shyichuk A, Sojka Z et al (2021) Green synthesis, structure, cations distribution and bonding characteristics of superparamagnetic cobalt-zinc ferrites nanoparticles for Pb (II) adsorption and magnetic hyperthermia applications. J Mol Liq 328:115375
11. Tatarchuk T, Bououdina M, Al-Najar B, Bitra RB (2019) Green and ecofriendly materials for the remediation of inorganic and

organic pollutants in water. In: Naushad Mu (ed) A new generation material graphene: applications in water technology. Springer International Publishing, Cham, pp 69–110

12. Tatarchuk T, Al-Najar B, Bououdina M, Ahmed MA (2019) Catalytic and photocatalytic properties of oxide spinels. Handbook of ecomaterials 3:1701–1750

13. Liu Y, Hsu J, Fu Y, Tsai K (2016) Preparation of Cu–Zn ferrite photocatalyst and it's application. Int J Hydrogen Energy 41:15696–15702

14. Karthik K, Dhanuskodi S, Gobinath C et al (2017) Photocatalytic and antibacterial activities of hydrothermally prepared CdO nanoparticles. J Mater Sci: Mater Electron 28:11420–11429

15. Abdel-Hamid Z, Rashad MM, Mahmoud SM, Kandil AT (2017) Electrochemical hydroxyapatite-cobalt ferrite nanocomposite coatings as well hyperthermia treatment of cancer. Mater Sci Eng, C 76:827–838

16. Wang G, Zhao D, Ma Y et al (2018) Synthesis and characterization of polymer-coated manganese ferrite nanoparticles as controlled drug delivery. Appl Surf Sci 428:258–263

17. Kombaiah K, Vijaya JJ, Kennedy LJ et al (2018) Okra extract-assisted green synthesis of CoFe2O4 nanoparticles and their optical, magnetic, and antimicrobial properties. Mater Chem Phys 204:410–419

18. Satheeshkumar MK, Kumar ER, Srinivas C et al (2019) Structural and magnetic properties of CuFe2O4 ferrite nanoparticles synthesized by cow urine assisted combustion method. J Magn Magn Mater 484:120–125

19. Deepty M, Srinivas C, Kumar ER et al (2019) XRD, EDX, FTIR and ESR spectroscopic studies of co-precipitated Mn–substituted Zn–ferrite nanoparticles. Ceram Int 45:8037–8044

20. Deepty M, Srinivas C, Babu KV et al (2018) Structural and electron spin resonance spectroscopic studies of MnxZn1- xFe2O4 (x= 0.5, 0.6, 0.7) nanoferrites synthesized by sol-gel auto combustion method. J Magn Magn Mater 466:60–66

21. Giri AK, Kirkpatrick EM, Moongkhamklang P et al (2002) Photomagnetism and structure in cobalt ferrite nanoparticles. Appl Phys Lett 80:2341–2343

22. Bouokkeze D, Massoudi J, Hzez W et al (2019) Investigation of the structural, optical, elastic and electrical properties of spinel LiZn2Fe3O8 nanoparticles annealed at two distinct temperatures. RSC Adv 9:40940–40955. https://doi.org/10.1039/C9RA07569K

23. Benali EM, Benali A, Bejar M et al (2020) Effect of annealing temperature on structural, morphological and dielectric properties of La0.8Ba0.1Ce0.1FeO3 perovskite. J Mater Sci: Mater Electron 31:16220–16234. https://doi.org/10.1007/s10854-020-04140-w

24. Massoudi J, Smari M, Nouri K et al (2020) Magnetic and spectroscopic properties of Ni–Zn–Al ferrite spinel: from the nanoscale to microscale. RSC Adv 10:34556–34580

25. Massoudi J, Messaoudi O, Gharbi S et al (2022) Magnetocaloric effect, dielectric relaxor behavior, and evidence for direct magnetodielectric behavior in Ni0. 6Zn0. 4Al0. 5Fe1. 5O4 ceramics for high-temperature applications. J Phys Chem C 126:2857–2867

26. Massoudi J, Smari M, Khirouni K et al (2021) Impact of particle size on the structural and smagnetic properties of superparamagnetic Li-ferrite nanoparticles. J Magn Magn Mater 528:167806. https://doi.org/10.1016/j.jmmm.2021.167806

27. Lahouli R, Massoudi J, Smari M et al (2019) Investigation of annealing effects on the physical properties of Ni 0.6 Zn 0.4 Fe 1.5 Al 0.5 O 4 ferrite. RSC Adv 9:19949–19964

28. Massoudi J, Bouekkeze D, Bougoffa A et al (2020) Structural, elastic, optical and dielectric properties of Li0.5Fe2.5 O4 nanopowders with different particle sizes. Adv Powder Technol 31:4714–4730

29. Gandomi F, Peymani-Motlagh SM, Rostami M et al (2019) Simple synthesis and characterization of Li0.5Fe2.5O4, LiMg0.5Fe2O4 and LiNi0.5Fe2O4, and investigation of their photocatalytic and anticancer properties on hela cells line. J Mater Sci: Mater Electron 30:19691–19702

30. Shirsath SE, Kadam RH, Mane ML et al (2013) Permeability and magnetic interactions in Co2+ substituted Li0.5Fe2.5O4 alloys. J Alloy Compd 575:145–151. https://doi.org/10.1016/j.jallcom.2013.04.058

31. Mabrouki A, Mnasri T, Bougoffa A et al (2021) Experimental study and DFT calculation of the oxygen deficiency effects on structural, magnetic and optical properties of La0.8□0.2MnO3-δ (δ = 0, 0.1 and 0.2) compounds. J Alloys Compd 860:157922. https://doi.org/10.1016/j.jallcom.2020.157922

32. Hajra P, Shyamal S, Mandal H et al (2019) Synthesis of oxygen deficient bismuth oxide photocatalyst for improved photoelectrochemical applications. Electrochim Acta 299:357–365

33. Trabelsi H, Bejar M, Dhahri E et al (2019) Oxygen-vacancy-related giant permittivity and ethanol sensing response in SrTiO3-δ ceramics. Physica E 108:317–325. https://doi.org/10.1016/j.physe.2018.12.025

34. Vaqueiro P, López-Quintela MA (1998) Synthesis of yttrium aluminium garnet by the citrate gel process. J Mater Chem 8:161–163

35. Kim Y-I, Izumi F (1994) Structure refinements with a new version of the Rietveld-Refinement program RIETAN. J Ceram Soc Jpn 102:401–404

36. Patil RP, Hankare PP, Garadkar KM, Sasikala R (2012) Effect of sintering temperature on structural, magnetic properties of lithium chromium ferrite. J Alloy Compd 523:66–71

37. Rahimi M, Kameli P, Ranjbar M, Salamati H (2013) The effect of sintering temperature on evolution of structural and magnetic properties of nanostructured Ni0. 3Zn0. 7Fe2O4 ferrite. J Nanopart Res 15:1–11

38. Prajapat P, Dhaka S, Mund HS (2021) Investigation of the influence of annealing temperature on the structural and magnetic properties of MgFe2O4. J Electron Mater 50:4671–4677

39. Waje SB, Hashim M, Yusoff WDW, Abbas Z (2010) Sintering temperature dependence of room temperature magnetic and dielectric properties of Co0. 5Zn0. 5Fe2O4 prepared using mechanically alloyed nanoparticles. J Magn Magn Mater 322:686–691

40. Maaz K, Karim S, Mumtaz A et al (2009) Synthesis and magnetic characterization of nickel ferrite nanoparticles prepared by co-precipitation route. J Magn Magn Mater 321:1838–1842

41. Gonçalves NS, Carvalho JA, Lima ZM, Sasaki JM (2012) Size–strain study of NiO nanoparticles by X-ray powder diffraction line broadening. Mater Lett 72:36–38

42. Kumar ER, Srinivas C, Seehra MS et al (2018) Particle size dependence of the magnetic, dielectric and gas sensing properties of Co substituted NiFe2O4 nanoparticles. Sens Actuators, A 279:10–16

43. Schneider CA, Rasband WS, Eliceiri KW (2012) NIH Image to ImageJ: 25 years of image analysis. Nat Methods 9:671–675

44. Soudani I, Brahim KB, Oueslati A et al (2022) Investigation of structural, morphological, and transport properties of a multifunctional Li-ferrite compound. RSC Adv 12:18697–18708. https://doi.org/10.1039/D2RA02757G

45. Sharma R, Bansal S, Singhal S (2015) Tailoring the photo-Fenton activity of spinel ferrites (MFe 2 O 4) by incorporating different cations (M= Cu, Zn, Ni and Co) in the structure. RSC Adv 5:6006–6018

46. Alagarasan D, Varadharajaperumal S, Kumar KDA et al (2021) Optimization of different temperature annealed nanostructured CdSe thin film for photodetector applications. Opt Mater 122:111706

47. Chavan AR, Vinayak V, Rathod SM, Khirade PP (2021) Diverse physical characteristics of mixed Li–Mg spinel ferrite thin films fabricated by spray pyrolysis technique. Physica B 615:413075

48. Sahoo D, Priyadarshini P, Aparimita A et al (2020) Role of annealing temperature on optimizing the linear and nonlinear optical properties of As 40 Se 50 Ge 10 films. RSC Adv 10:26675–26685

49. Li X, Zhu H, Wei J et al (2009) Determination of band gaps of self-assembled carbon nanotube films using Tauc/Davis–Mott model. Appl Phys A 97:341–344

50. Hadded A, Massoudi J, Dhahri E et al (2020) Structural, optical and dielectric properties of $Cu_{1.5}Mn_{1.5}O_4$ spinel nanoparticles. RSC Adv 10:42542–42556. https://doi.org/10.1039/D0RA08405K

51. Hannachi L, Bouarissa N (2009) Band parameters for cadmium and zinc chalcogenide compounds. Physica B 404:3650–3654

52. Turky AO, Rashad MM, Hassan AM et al (2017) Optical, electrical and magnetic properties of lanthanum strontium manganite La 1–x Sr x MnO3 synthesized through the citrate combustion method. Phys Chem Chem Phys 19:6878–6886

53. Ravindra NM, Srivastava VK (1979) Variation of electronic polarizability with energy gap in compound semiconductors. Infrared Phys 19:605–606

54. Rahmouni H, Smari M, Cherif B et al (2015) Conduction mechanism, impedance spectroscopic investigation and dielectric behavior of La 0.5 Ca 0.5- x Ag x MnO 3 manganites with compositions below the concentration limit of silver solubility in perovskites (0≤ x≤ 0.2). Dalton Trans 44:10457–10466

55. Dhahri A, Zaouali A, Benali A et al (2021) Synthesis and study of the structural and dielectric properties of La0. 67Ca0. 2Ba0. 13Fe1- xMnxO3 ferrites (x= 0, 0.03 and 0.06). J Mater Sci: Mater Electron 32:7926–7942

56. Benali A, Bejar M, Dhahri E et al (2015) Electrical conductivity and ac dielectric properties of La0. 8Ca0. 2-xPbxFeO3 (x= 0.05, 0.10 and 0.15) perovskite compounds. J Alloy Compd 653:506–512

57. Baaziz H, Maaloul NK, Tozri A et al (2015) Effect of sintering temperature and grain size on the electrical transport properties of La0. 67Sr0. 33MnO3 manganite. Chem Phys Lett 640:77–81

58. Bharti C, Sinha TP (2011) Structural and ac electrical properties of a newly synthesized single phase rare earth double perovskite oxide: Ba2CeNbO6. Physica B 406:1827–1832

59. Dutta A, Bharti C, Sinha TP (2008) Dielectric relaxation in Sr (Mg1/3Nb2/3) O3. Physica B 403:3389–3393

60. Abdallah FB, Benali A, Triki M et al (2018) Effect of annealing temperature on structural, morphology and dielectric properties of La0. 75Ba0. 25FeO3 perovskite. Superlattices Microstruct 117:260–270

61. Felhi H, Lahouli R, Smari M et al (2019) Study of the structural, electric and dielectric proprieties of Bi1-xNdxMn2O5 (x= 0, x= 0.1 and x= 0.2). J Mol Struct 1179:1–10

62. Amghar M, Bougoffa A, Trabelsi A et al (2022) Structural, morphological, and electrical properties of silver-substituted ZnAl 2 O 4 nanoparticles. RSC Adv 12:15848–15860

63. Yahya SB, Louati B (2021) Characterization of the structure and conduction behavior of overlapping polaron tunnel of dipotassium zinc orthogermanate. J Alloy Compd 876:159972. https://doi.org/10.1016/j.jallcom.2021.159972

64. Louati B, Guidara K (2011) Dielectric relaxation and ionic conductivity studies of LiCaPO4. Ionics 17:633–640

65. Nasri M, Henchiri C, Dhahri R et al (2021) Structural, dielectric, electrical and modulus spectroscopic characteristics of CoFeCuO4 spinel ferrite nanoparticles. Mater Sci Eng, B 272:115331. https://doi.org/10.1016/j.mseb.2021.115331

66. Hamdaoui N, Azizian-Kalandaragh Y, Khlifi M, Beji L (2019) Structural, magnetic and dielectric properties of Ni0.6Mg0.4Fe2O4 ferromagnetic ferrite prepared by sol gel method. Ceram Int 45:16458–16465. https://doi.org/10.1016/j.ceramint.2019.05.177

67. Pandit AA, Shitre AR, Shengule DR, Jadhav KM (2005) Magnetic and dielectric properties of Mg1+ x Mn x, Fe2- 2x, O4 ferrite system. J Mater Sci 40:423–428

68. Hcini S, Selmi A, Rahmouni H et al (2017) Structural, dielectric and complex impedance properties of T0. 6Co0. 4Fe2O4 (T= Ni, Mg) ferrite nanoparticles prepared by sol gel method. Ceram Int 43:2529–2536

69. Ravinder D (1999) Effect of sintering temperature on electrical conductivity of mixed lithium–cadmium ferrites. Mater Lett 40:198–203

70. Bougoffa A, Benali A, Bejar M et al (2021) Mg-substitution effect on microstructure, dielectric relaxation and conduction phenomenon of Fe based perovskite nanomaterials. J Alloy Compd 856:157425

71. Oumezzine E, Hcini S, Rhouma FIH, Oumezzine M (2017) Frequency and temperature dependence of conductance, impedance and electrical modulus studies of Ni0. 6Cu0. 4Fe2O4 spinel ferrite. J Alloy Compd 726:187–194

72. Rahman KR, Chowdhury F-U-Z, Khan MNI (2017) Influence of Al3+ substitution on the electrical resistivity and dielectric behavior of Ni0. 25Cu0. 20Zn0. 55AlxFe2-xO4 ferrites synthesized by solid state reaction technique. J Magn Magn Mater 443:366–373

73. Devan RS, Kolekar YD, Chougule BK (2006) Effect of cobalt substitution on the properties of nickel–copper ferrite. J Phys: Condens Matter 18:9809